Paleoceanography and Paleoclimatology®

RESEARCH ARTICLE
10.1029/2020PA004183

Key Points:

- The Last Glacial Maximum (LGM) Antarctic Circumpolar Current (ACC) baroclinic transport can be reconstructed using only end-member water masses at Australian margin
- One additional direct measurement below Antarctic Intermediate Water (AAIW) depth is essential to reconstruct the correct sign of change in transport at the LGM
- The uncertainty in transport reconstruction is large when salinities of Subtropical Surface Water and AAIW are reconstructed independently

Supporting Information:

Supporting Information may be found in the online version of this article.

Correspondence to:

L. Li and Z. Liu,
li.8955@osu.edu;
liu.7022@osu.edu

Citation:

Li, L., Liu, Z., Lynch-Stieglitz, J., He, C., Gu, S., Zhang, J., & Otto-Bliesner, B. (2021). Testing methods for reconstructing glacial Antarctic Circumpolar Current transport in an isotope-enabled climate model. *Paleoceanography and Paleoclimatology*, *36*, e2020PA004183. https://doi.org/10.1029/2020PA004183

Received 4 DEC 2020
Accepted 27 SEP 2021

Testing Methods for Reconstructing Glacial Antarctic Circumpolar Current Transport in an Isotope-Enabled Climate Model

Lingwei Li[1], Zhengyu Liu[1], Jean Lynch-Stieglitz[2], Chengfei He[1], Sifan Gu[3], Jiaxu Zhang[4,5], and Bette Otto-Bliesner[6]

[1]Atmospheric Science Program, Department of Geography, The Ohio State University, Columbus, OH, USA, [2]School of Earth and Atmospheric Sciences, Georgia Institute of Technology, Atlanta, GA, USA, [3]School of Oceanography, Shanghai Jiao Tong University, Shanghai, People's Republic of China, [4]Cooperative Institute for Climate, Ocean, and Ecosystem Studies, University of Washington, Seattle, WA, USA, [5]NOAA/Pacific Marine Environmental Laboratory, Seattle, WA, USA, [6]Climate and Global Dynamics Division, National Center for Atmospheric Research, Boulder, CO, USA

Abstract The Antarctic Circumpolar Current (ACC) plays a vital role in the interbasin exchange of ocean properties. A robust method to reconstruct the ACC baroclinic transport is helpful to assess the ACC's sensitivity to a changed climate. Here we test the reconstruction methods at the Last Glacial Maximum (LGM; ~20 ka) using end-member water masses in a fully coupled, isotope-enabled Community Earth System Model. Model results suggest that the density profile at the northern side of ocean margins across the ACC can be reconstructed well from end-member water masses of Subtropical Surface Water (STSW), Antarctic Intermediate Water (AAIW), and Lower Circumpolar Deep Water. One additional pore fluid observation at 1,000 m can substantially improve transport reconstruction and is essential to constrain the sign of change in ACC transport during the LGM. Moreover, the uncertainty in transport calculation is large when salinities for STSW and AAIW are reconstructed independently based on the $\delta^{18}O_{sw}$-Salinity relationship of surface and intermediate waters in the South Indian Ocean. More direct measurements of LGM temperature and salinity may allow better transport reconstruction.

Plain Language Summary The Antarctic Circumpolar Current (ACC) in the Southern Ocean is important in the interbasin exchange of ocean properties through its horizontal circulation. Most of this flow is associated with seawater density gradients (the baroclinic transport). Therefore, a robust method that can be used to reconstruct the ACC baroclinic transport is the key to understand the sensitivity of the ACC to paleoclimate conditions. Here we test the method to reconstruct the ACC baroclinic transport during the Last Glacial Maximum (LGM; ~20 ka) using water mass properties from surface water, intermediate water and deep water end members. Results from a fully coupled, isotope-enabled Community Earth System Model suggest that the density profile at the northern side of ocean margins across the ACC can be reconstructed well from end-member water masses. And one additional pore fluid observation at intermediate depth can improve transport reconstruction and constrain the sign of change in ACC transport during the LGM. However, the uncertainty in transport estimation is large when salinities for water masses are further reconstructed. More direct measurements of LGM temperature and salinity may allow better transport reconstruction.

1. Introduction

The Antarctic Circumpolar Current (ACC) in the Southern Ocean (SO) is a vital component of the global ocean and climate system since it plays a key role in the air-sea exchange of heat and carbon (Le Quere et al., 2007; Sabine et al., 2004). The storage and distribution of heat and carbon rely both on the horizontal circulation of the ACC and the overturning circulation coupled to it (Rintoul et al., 2001). The zonal geostrophic transport is predominantly baroclinic transport associated with the density structure (or the tilted isopycnals), which is determined, in turn, by the large-scale wind forcing (Gnanadesikan & Hallberg, 2000; Marshall & Radko, 2003), buoyancy forcing (Sun et al., 2016), and the resulted eddies (Farneti et al., 2010; Marshall et al., 2017). The baroclinic component of ACC transport has been monitored by World Ocean

Circulation Experiment (WOCE), which is measured to be 136.7 ± 7.8 Sverdrup (Sv; 1 Sv = 10^6 m^3s^{-1}) relative to zero at bottom for the 1993–2000 period (Cunningham et al., 2003; Rintoul & Sokolov, 2001).

During the Last Glacial Maximum (LGM) between ~23 and ~19 ka, the Antarctic temperature was estimated to be lower than the present day by up to 10°C (Jouzel et al., 2007), with more extensive ice sheets than the present day (Clark et al., 2009). The cold climate let to an enhanced stratification of the ocean, which has been hypothesized to explain reduced CO_2 outgassing (Burke & Robinson, 2012; Sigman et al., 2010). Consequently, an estimate of the baroclinic transport of the LGM ACC is needed to assess how carbon was stored and transported in this cold climate. Physically, the ACC baroclinic transport can be inferred by density stratification because the ACC is in thermal wind balance. However, it remains challenging to reconstruct the density structure of the SO at the LGM. Due to the sparsity of proxy data and the uncertainties of reconstruction methods, current proxy-based reconstructions yield controversial results. For example, one study suggests a total reduction of transport at Drake Passage based on measurements of sortable silt grain size (Lamy et al., 2015), while another study finds no net change in transport around the Drake Passage based on the same method (McCave et al., 2014). Modeling studies also show a wide range for the ACC transport. Models that participated in the Paleoclimate Model Intercomparison Project (PMIP) Phase 2 (Braconnot et al., 2007) and Phase 3 (Braconnot et al., 2012) show large (to order-of-magnitude) intermodal spread in ACC transport from 40 to 300 Sv. Therefore, a robust approach is required to estimate the ACC baroclinic transport during the LGM, which will shed light on the ACC's sensitivity to a changed climate.

Stable oxygen isotope ($\delta^{18}O$) in the benthic foraminifera ($\delta^{18}O_c$) provides a potential method to reconstruct the past seawater density to infer the oceanic transport change (Gu et al., 2019; Lynch-Stieglitz et al., 2006). This is because, first, $\delta^{18}O_c$ is one of the most abundant proxy observations and, second, $\delta^{18}O_c$ is determined by the temperature and $\delta^{18}O$ of seawater ($\delta^{18}O_{sw}$), the latter of which is often linearly correlated with salinity (Craig et al., 1965; LeGrande & Schmidt, 2011). However, $\delta^{18}O_c$ cannot be used directly to estimate density in the SO under the cold LGM climate because the relationship between $\delta^{18}O_{sw}$ and salinity is altered by the sea ice formation, which is extensive in the SO at the LGM (Brennan et al., 2013; Toyota et al., 2013). Lynch-Stieglitz et al. (2016) proposed a reconstruction method (hereafter LS16) that reconstructs the ACC baroclinic transport from two vertical density profiles across the ACC along the Australia section; the density profiles are reconstructed from the temperature and salinity properties of the end-member water masses and the vertical profiles of the $\delta^{18}O_c$ from sediment cores. This method is plausible because the measured modern $\delta^{18}O_{sw}$-Salinity (S)-Temperature (T) relationship can be approximated as a linear relation due to mixing between pairs of the three end-member water masses: Subtropical Surface Water (STSW) formed within the subtropical gyre, Antarctic Intermediate Water (AAIW) found mostly at intermediate depths in the SO with relatively low salinity, and Lower Circumpolar Deep Water (LCDW) formed by a mixture of deep waters. With independent estimation of temperature and salinity of each end-member water masses, the density profile can be reconstructed, and hence the transport can be estimated.

This method, nevertheless, relies on several key assumptions. First, the $\delta^{18}O_{sw}$-S-T relationship is assumed to be controlled by similar linear mixing process at the LGM as today. Second, since no pore water measurements are available for AAIW and STSW, properties of end-members AAIW and STSW have to be estimated independently at the LGM. Therefore, paleosalinities of end-member water masses should be further reconstructed based on the linear $\delta^{18}O_{sw}$-S relationship of surface and intermediate water in the South Indian Ocean. It assumes that the $\delta^{18}O_{sw}$-S relationship between STSW and AAIW in the SO can be well reproduced in the South Indian Ocean, as the result of mixing between subtropical gyre water and high-latitude freshwater end-member, and this linear $\delta^{18}O_{sw}$-S relationship of the present day holds during the LGM. These assumptions render the LS16 method to potential uncertainties. While the uncertainties in the LGM end-members were considered in LS16 and propagated into the uncertainty in the LGM transport, it is assumed that the end-member mixing structure held for the LGM.

This paper will assess the uncertainty of the LS16 method in the reconstruction of the ACC baroclinic transport. We will assess the method in the context of an isotope-enabled coupled climate model that allows for direct model-proxy comparison, with the objective of suggesting possible improvements in the reconstruction method. We find that end-member water masses can be used to reconstruct the vertical density profile reasonably well, and the reconstruction can be substantially improved by one additional pore water observations below the AAIW depth. This study is structured as follows. Section 2 describes the models and

Table 1
PMIP3 Models Used in This Study

Climate model	Institution	Country	Horizontal resolution	References
CNRM-CM5	Centre National de Researches Meterologiques	France	292 × 362	Voldoire et al. (2013)
FGOALS-G2	Laboratory of Numerical Modeling for Atmospheric Sciences and Geophysical Fluid Dynamics	China	196 × 360	Li et al. (2013)
MIROC-ESM	Atmosphere and Ocean Research Institute	Japan	192 × 256	Watanabe et al. (2011)
MRI-CGCM3	Meterological Research institute	Japan	368 × 360	Yukimoto et al. (2012)
CCSM4	National Center for Atmospheric Research	United States	384 × 320	Gent et al. (2011)

data used in the study. Section 3 introduces the series of reconstruction methods to be tested. The major results are presented in Sections 4–6. Section 4 tests methods to reconstruct the baroclinic transport using observed paleo density profiles; Section 5 tests methods in which observational conditions are relaxed to have paleo density observations only for end-members water masses; Section 6 further tests methods in which paleo-density observations are only available for the deepest end-member water mass. Finally, a summary is given in Section 7.

2. Model and Data

We use the output from a water isotope-enabled ($\delta^{18}O$, δD), fully coupled Community Earth System Model (iCESM) version 1.3 (Brady et al., 2019). The iCESM includes the atmosphere, ocean, land, sea ice, and river runoff components with stable water isotopes incorporated to facilitate a direct model-data comparison (Brady et al., 2019; Zhang et al., 2017). The ocean component uses the Parallel Ocean Program version 2 (Smith et al., 2010), which has a nominal 1° horizontal resolution (gx1v6) and 60 vertical layers with a 10 m resolution in the upper 160 m expanding to a 250 m resolution below 3,500 m. Here, we use the output from two experiments, the pre-industrial (PI, ~1,850) and the LGM (~20.0 ka) experiments (He et al., 2021a, 2021b). The model is able to simulate both the physical aspects of the present-day climate and water isotopes in the atmosphere and ocean reasonably well (Hurrell et al., 2013; Zhang et al., 2017). The LGM simulation in the iCESM shows colder global mean temperature up to 7°C compared to the PI simulation, which agrees with the upper range of one reconstruction (Snyder, 2016).

We also use the output from five PMIP3 models (Braconnot et al., 2012) for assessing the reconstruction of the baroclinic transport using the vertical density profiles (Table 1). Each PMIP3 model only considers one ensemble member (r1i1p1) and has both "piControl" and "LGM" experiments with ocean potential temperature "thetao," salinity "so," and seawater velocity "uo" and "vo" monthly fields available. For each model, the "piControl" simulation is used as the control run compared against the "LGM" experiment. Annual mean climatology was calculated for analysis and potential density was calculated from the salinity and temperature fields to estimate the ACC baroclinic transport.

3. Methods

In this section, we briefly introduce a series of methods for a systematic test of the reconstruction of the baroclinic transport of the ACC (Table 2), while the details of each method will be discussed later in Sections 4–6. Largely following the idea of LS16, this series of methods are staggered in three steps with increased degrees of approximation to meet the presumably increased restrictions toward realistic paleo-observation scenarios. We also explore methods that can improve the estimation by incorporating limited new observations. In Step 1, we assume that we have only 2, or even 1, vertical profiles of ocean density observation on the ocean margins across the ACC. The density profiles can be used to calculate approximately the meridional density gradient and, in turn, the baroclinic ACC transport using the thermal wind relation, which is the dynamic base for the reconstruction. In Step 2, we further assume that the density observation is limited to only a few end-member water masses on the northern margin of the ACC. Now, the vertical density profile at this site will be reconstructed by first estimating the T and S of end-member water masses

Table 2
Methods for Reconstructing ACC Baroclinic Transport in the iCESM

Steps	Methods	Transports (Sv)
Truth	Model baroclinic transport $u_z = u_{z0} + \frac{g}{\rho_o f}\int_{zo}^{z}\frac{\partial\rho}{\partial y}dz$	$T_{Truth,\ PI} = 99.2$ $T_{Truth,\ LGM} = 242.3$
Step 1 (S1)	S1_M1: Using both north and south margin density profiles $u_z = u_{z0} + \frac{g}{\rho_0 f}\int_{z0}^{z}\frac{\rho_S - \rho_N}{\Delta y}dz$	$T_{S1\_M1,\ PI} = 101.4$ $T_{S1\_M1,\ LGM} = 223.1$
	S1_M2: Using only north margin density profile $u_z = u_{z0} + \frac{g}{\rho_0 f}\int_{z0}^{z}\frac{\rho_{N,3.3km} - \rho_N}{\Delta y}dz$	$T_{S1\_M2,\ PI} = 108.1$ $T_{S1\_M2,\ LGM} = 168.6$
Step 2 (S2)	S2_M1: Using end-member water masses and $\delta^{18}O_c$ profile as weight to reconstruct the north margin density profile $(\rho_N)\ u_z = u_{z0} + \frac{g}{\rho_0 f}\int_{z0}^{z}\frac{\rho_{N,3.3km} - \rho_N}{\Delta y}dz$	$T_{S2\_M1,\ PI} = 77.3$ $T_{S2\_M1,\ LGM} = 67.4$
	S2_M2: Using end-member water masses and one additional pore fluid at 1 km to reconstruct the north margin density profile $(\rho_N)\ u_z = u_{z0} + \frac{g}{\rho_0 f}\int_{z0}^{z}\frac{\rho_{N,3.3km} - \rho_N}{\Delta y}dz$	$T_{S2\_M2,\ PI} = 88.8$ $T_{S2\_M2,\ LGM} = 103.5$
Step 3 (S3)	S3_M1: Using end-member water masses with salinities of STSW and AAIW are further reconstructed to get the north margin density profile $(\rho_N)\ u_z = u_{z0} + \frac{g}{\rho_0 f}\int_{z0}^{z}\frac{\rho_{N,3.3km} - \rho_N}{\Delta y}dz$	$T_{S3\_M1,\ PI} = 73.5 \pm 35.1$ $T_{S3\_M1,\ LGM} = 37.6 \pm 35.0$

Note. Transport calculation with equations for geostrophic shear are attached for each method. u is the zonal velocity components; u_{z0} is the velocity at the reference level; g is the gravitational acceleration; ρ_0 is the reference seawater density; f is the Coriolis Parameter; $\Delta y/\partial y$ is the meridional width; ρ_N is the northern (40°S) margin potential density profile; ρ_S is the southern (60°S) margin potential density profile; $\rho_{N,\ 3.3km}$ is the assumed constant southern margin density profile with the density further approximated by that at the LCDW depth (3.3 km) of the northern margin profile. Both calculations use 3.3 km as the level of no motion ($u_{z0} = 0$ at $z0 = 3.3$ km). AAIW, Antarctic Intermediate Water; ACC, Antarctic Circumpolar Current; iCESM, isotope-enabled Community Earth System Model; LCDW, Lower Circumpolar Deep Water; LCM, Last Glacial Maximum; STSW, Subtropical Surface Water.

and then combining these end-member properties with vertical profiles of $\delta^{18}O_c$. In Step 3, we further relax the observation. We assume that we only have the density observation in the single abyssal end-member LCDW while other end-members need to be estimated independently.

More specifically, in Step 1 (S1), we start with the most ideal case that we have the observation of vertical density profiles. In the first case, we assume we have two vertical profiles on both the northern and southern sides of the ocean margin across the ACC along, for example, the Australia sector (AU, 135°E) as showed in Figure 1. This case corresponds to method S1_M1 (Table 2). In the second case, the observational condition is relaxed such that we only have the single density profile on the northern side. The southern density profile is approximated as a constant profile with the density further approximated by that at the bottom (LCDW) depth of the northern profile, because they both are assumed approximately to represent the LCDW water mass. This case corresponds to method S1_M2 (Table 2). Both methods in this step have been tested in the PMIP2 output to be largely successful (Lynch-Stieglitz et al., 2016). Here, these methods will be tested further in the most recent PMIP3 simulations and will be further improved in their formulation, as will be discussed in detail in Section 4.

The focus of our paper is on the next two steps that are based on observations of end-members and oxygen water isotopes. In Step 2 (S2), we assume that, on the northern margin, the observation of the entire vertical density profile is further relaxed such that we only have the observations of water densities for several end-member water masses. This would correspond to having pore fluid observations and $\delta^{18}O_c$ for each water mass from which temperature and salinity could be inferred. In S2 we also presume that we have a vertical profile of $\delta^{18}O_c$ on the northern margin site, presumably from measurements on benthic foraminifera. We then can reconstruct the density profile using water property of the end-member water masses and the

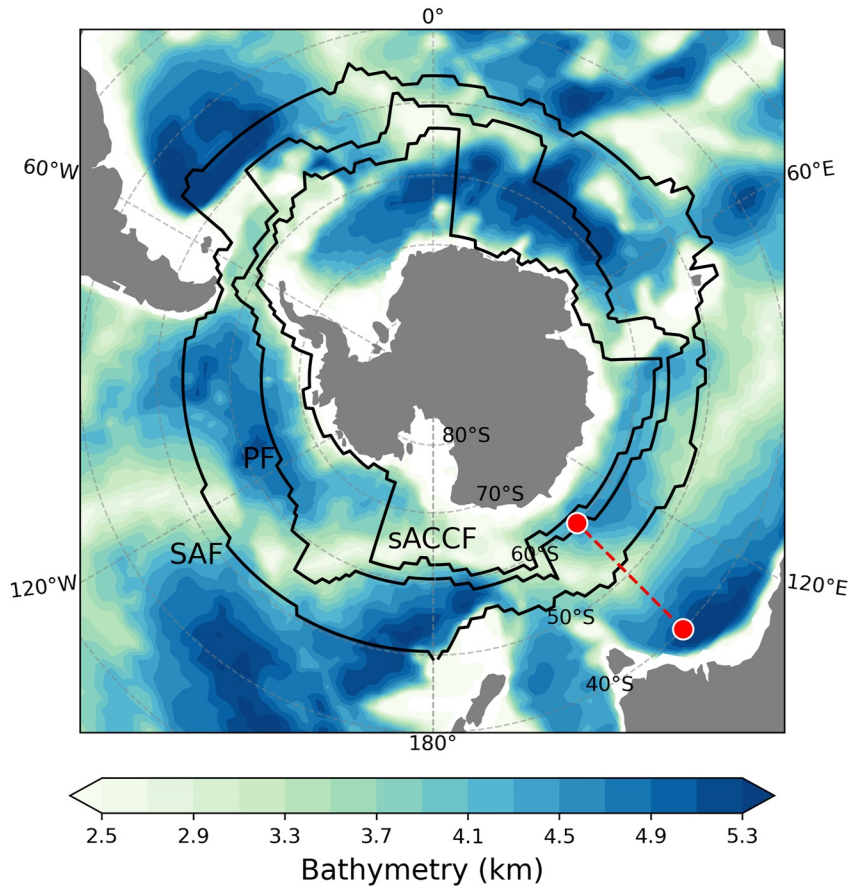

Figure 1. Locations of the Australia section (red dashed line) and the density profiles used in the Antarctic Circumpolar Current density reconstruction (red dots). Solid black lines are the position of the Antarctic Fronts from the pre-industrial simulation of the isotope-enabled Community Earth System Model: the Subantarctic Front (SAF), Polar Front (PF), and Southern Antarctic Circumpolar Current Front (sACC). Bathymetry (km) deeper than 2.5 km is shaded in the background. The definitions of the Antarctic Fronts follow Orsi et al. (1995) along specific features in the potential temperature field.

vertical profile of $\delta^{18}O_c$ to weight the proportion of end-member waters at each depth. We first discuss the case where we have the water properties for three end-members STSW, AAIW, and LCDW, corresponding to method S2_M1 (Table 2). We then discuss a case, corresponding to method S2_M2, in which the estimation can be substantially improved, if we have one additional pore fluid observation at ~1 km depth. The details of this step are discussed in Section 5.

In Step 3 (S3), we further relax the observational condition from Step 2 such that pore water based estimates of temperature and salinity are available only in the deepest end-member, LCDW (Adkins et al., 2002) and, thus, paleo-salinities of STSW and AAIW must be reconstructed independently from the linear $\delta^{18}O_{sw}$-S relationship of surface and intermediate waters in the South Indian Ocean. It is assumed that this $\delta^{18}O_{sw}$-S relationship is the result of mixing between subtropical gyre waters and a high-latitude freshwater end-member, and that this is also the case during the LGM. This method is denoted as S3_M1 and is tested in our fully coupled model experiments. The details of this step are discussed in Section 6.

4. Reconstructing Baroclinic Transport Using Site Density Profile

We first test methods of Step 1 using horizontal (S1_M1) and vertical (S1_M2) density stratification to calculate the ACC baroclinic transport. These tests confirm that the vertical density stratification alone along the northern margin can be used to estimate the baroclinic transport. The S1_M1 method here uses two vertical

density profiles on both the northern (40°S) and southern (60°S) sides of the ocean margin across the ACC along the AU sector such that the geostrophic shear is calculated as

$$u_z = u_{z0} + \frac{g}{\rho_0 f}\int_{z0}^{z}\frac{\rho_S - \rho_N}{\Delta y}dz \quad (1)$$

where u is the zonal velocity component; u_{z0} is the velocity at the reference level (3.3 km), which is assumed to be zero; g is the gravitational acceleration; ρ_0 is the reference seawater density; f is the Coriolis Parameter; ρ_N is the northern (40°S) margin potential density profile; ρ_S is the southern (60°S) margin potential density profile; and Δy is the meridional width from 60°S to 40°S. The depth 3.3 km is chosen as the reference level, consistent with LS16, because there is no topographic barrier between the Antarctic and Australian continent at this depth south of Australia, and the model velocity at this depth is nearly zero in the model at AU sector. The depth 3.3 km here is also nearly the depth of minimum geostrophic shear such that the transport calculation is least sensitive to the chosen reference level (Lynch-Stieglitz, 2001; Wunsch, 1996). In the second case S1_M2, we use only one north margin density profile

$$u_z = u_{z0} + \frac{g}{\rho_0 f}\int_{z0}^{z}\frac{\rho_{N,3.3km} - \rho_N}{\Delta y}dz \quad (2)$$

where $\rho_{N,\,3.3km}$ is the assumed constant southern margin density profile with the density further approximated by that at the bottom (LCDW) depth of the northern profile.

Our tests with iCESM and PMIP3 experiments confirm that the horizontal density gradient, or even the vertical density stratification in the northern margin alone, can be used to estimate the baroclinic transport. As shown in the scatter diagram in Figure 2a, the estimated transport using S1_M1 is in excellent agreement with the true baroclinic transport, as the points are arrayed along a 1:1 line (cross-correlation $r = 0.996$). This suggests that the ACC transport can be estimated using the cross-ACC density difference. The estimated transport in S1_M2 also reproduces the modeled baroclinic transport reasonably well (Figure 2b, $r = 0.960$), although the estimation is deteriorated somewhat relative to S1_M1. Furthermore, the transport, and the difference in transport between LGM and PI, in S1_M2 is also correlated with the estimation in S1_M1 (Figures 2c and 2d). This suggests that the northern density profile alone can be used to estimate the ACC transport. This result further supports the conclusion of LS16 based on the PMIP2 experiments.

Physically, the correlation of S1_M2 with S1_M1 suggests that the ACC baroclinic transport is linked with the vertical density stratification as the vertical density gradient reflects the horizontal density gradient due to the oceanic subduction process. A further examination shows that the deviation in S1_M2 is mostly due to the imperfect assumption of the constant southern margin density profile in S1_M2 (Figure 3). In Figure 3, we show the density profiles in S1_M1 and S1_M2 in the World Ocean Atlas 2009 (WOA09) (Antonov et al., 2010; Locarnini et al., 2010) and iCESM PI and LGM simulations. Compared with WOA09, the PI simulation shows a more stratified potential density profile (Figures 3a and 3b), which might be explained by the relatively coarse bottom topography and the lack of eddy fields in the ocean component of iCESM to balance the wind forcing, potentially affecting the dynamics of the ACC and associated transport (Olbers et al., 2004; Rintoul et al., 2001). Nevertheless, both WOA09 and the iCESM PI simulation show that the assumed constant southern margin density in S1_M2 is greater than the density in S1_M1, especially in the upper ocean, thereby leading to a greater density gradient in S1_M2 than in S1_M1 (Figures 3a and 3b). The calculated PI baroclinic transport in S1_M2 thus is higher than the transport in S1_M1 (Figure S1 in Supporting Information S1). By contrast, the density gradient in S1_M2 is smaller than that in S1_M1 during the LGM (Figure 3c) so that the transport in S1_M2 is estimated to be smaller than the transport in S1_M1 (Figure S1 in Supporting Information S1). This inconsistency of southern margin density profiles in S1_M1 and S1_M2 suggests that the south margin density is slightly stratified, instead of uniform as assumed. The stratified south margin density is also examined in PMIP3 (Figure S2 in Supporting Information S1), indicating the imperfect assumption of south margin density profile in S1_M2 in all models, which can deteriorate the transport estimation relative to the S1_M1.

The formulation of the transport estimation can be further improved. In LS16, the Coriolis parameter uses today's average ACC latitude (56°S) with a 1-sigma uncertainty of ±2.5° latitude for the LGM

$$f = 2\Omega\sin(f) \quad (3)$$

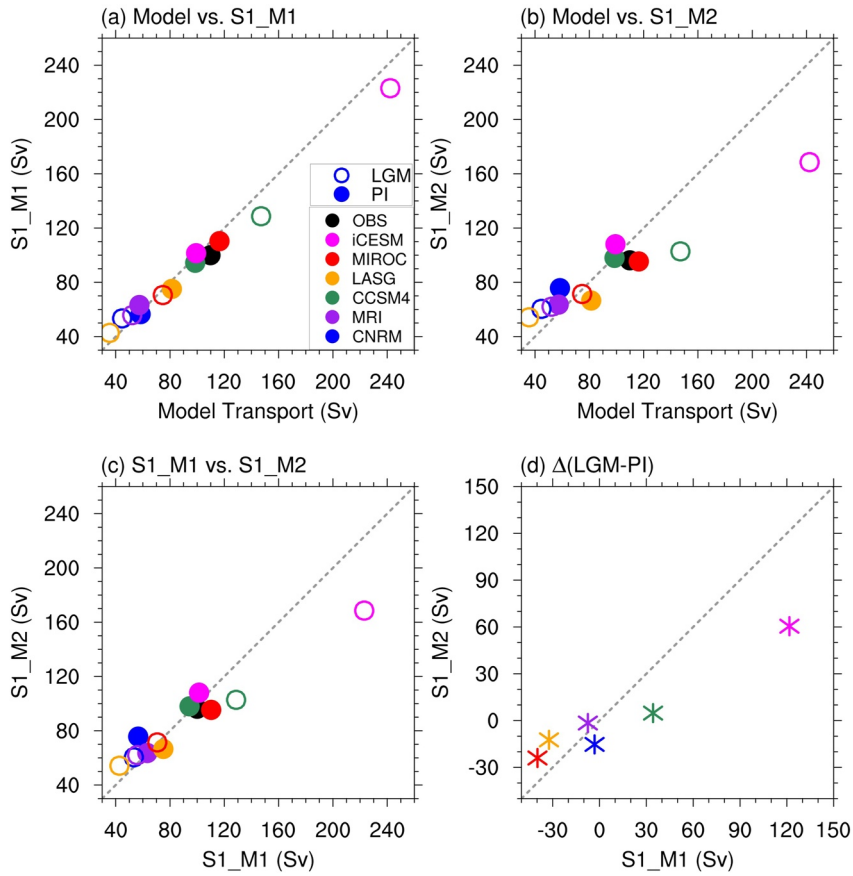

Figure 2. (a) The model baroclinic transport south of Australia (AU, 135°E) in the isotope-enabled Community Earth System Model and PMIP3 against the transport estimation in S1_M1 using north (40°S) and south (60°S) margin density profiles at the pre-industrial (PI) (solid circles) and Last Glacial Maximum (LGM) (open circles). (b) The model baroclinic transport against the transport estimation in S1_M2 using north margin density profile only. (c) The transport in S1_M1 against that in S1_M2. (d) The calculated transport difference (LGM-PI) in S1_M1 against that in S1_M2. The modern observations are from World Ocean Atlas 2009 (Antonov et al., 2010; Locarnini et al., 2010).

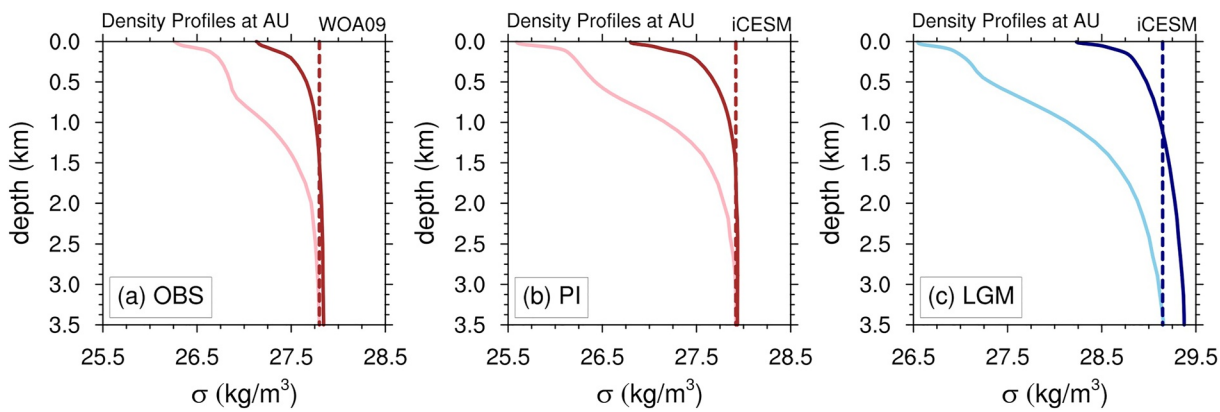

Figure 3. The potential density profiles around Australia sector in the (a) WOA09 and isotope-enabled Community Earth System Model (iCESM) (b) pre-industrial and (c) Last Glacial Maximum simulations. Dark color refers to the south margin (60°S) density profile and light color refers to the north margin (40°S) density profile. The dash lines refer to the assumed constant south margin density profile in S1_M2.

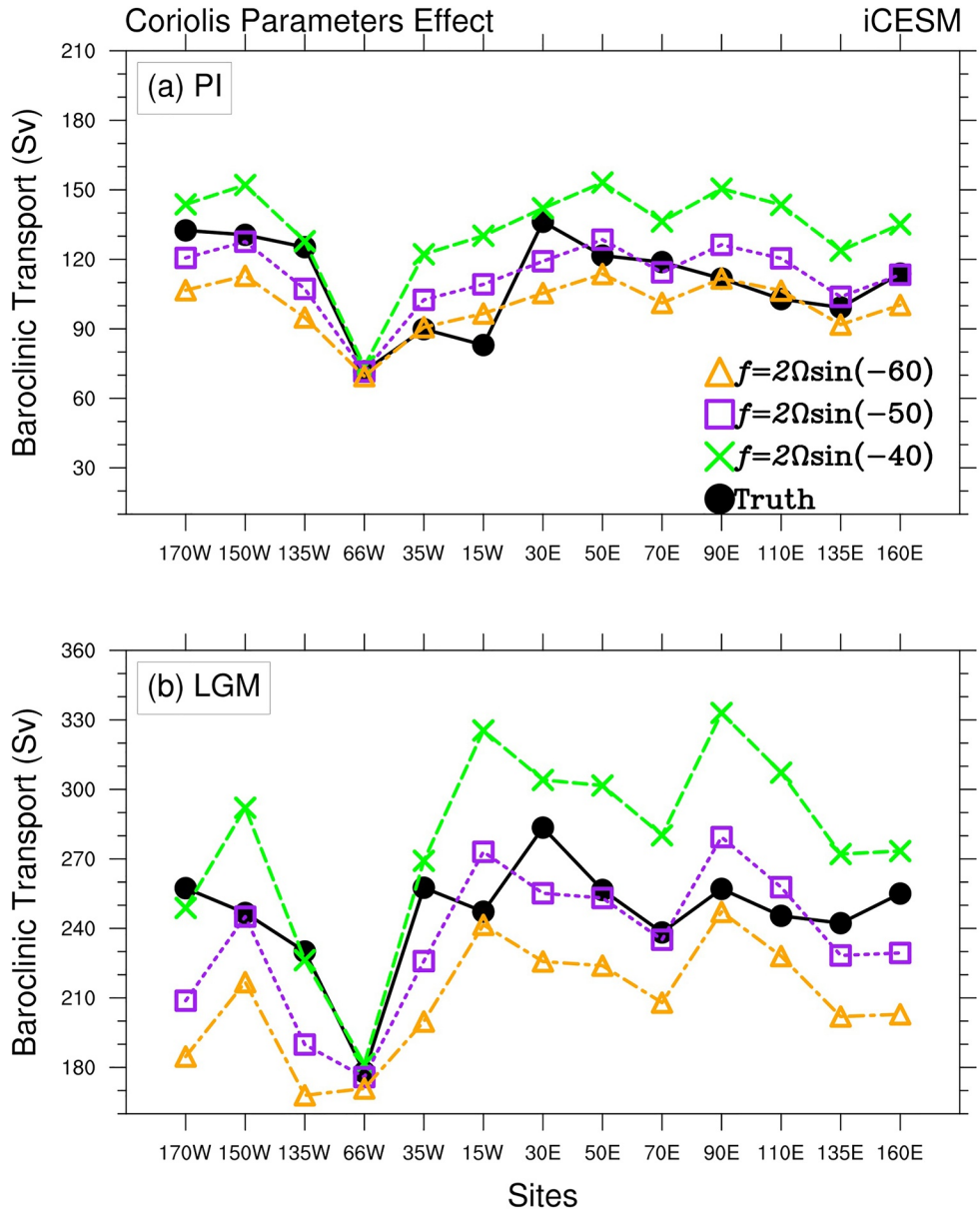

Figure 4. The model baroclinic transport (Truth, black) and transport estimation in S1_M1 using different Coriolis Parameters, calculated by the latitude 40°S (green), 50°S (purple), and 60°S (orange), across 13 sites along the Antarctic Circumpolar Current during the (a) pre-industrial and (b) Last Glacial Maximum. The Drake Passage (66°W) uses Coriolis parameters calculated by the latitude 57°S, 60°S, and 63°S due to its narrow channel.

where Ω is the angular speed of the earth and f is the latitude 56°S. Here our best estimate for the Coriolis parameter yields the latitude of 50°S in Equation 3 to calculate the geostrophic shear. Figure 4 shows the effect of the Coriolis parameter on the estimate of baroclinic transport in the iCESM. We use the most northern latitude 40°S, the midpoint latitude 50°S, and the most southern latitude 60°S for the Coriolis parameter in S1_M1 (Equation 1) across 13 sites along with the ACC, with f being the latitude 40°S, 50°S, and 60°S in Equation 3, respectively. Drake Passage (66°W) uses latitudes of 57°S, 60°S, and 63°S for Coriolis parameter calculation (Equation 3) due to its narrow meridional boundary. The overall percent error is then calculated as follow

$$\frac{1}{n}\sum_{i=0}^{n}\frac{\left|\mathrm{T}_{\mathrm{S1\_M1},f}(i)-T_{\mathrm{truth}}(i)\right|}{T_{\mathrm{truth}}(i)} \tag{4}$$

where $n = 13$ is the number of sites used, $T_{S1\_M1,f}$ is the S1_M1 transport estimated with different Coriolis parameters f, and T_{truth} is the model baroclinic transport at 13 sites along with the ACC. As shown in Figure 4, the Coriolis parameter that gives the transport estimation close to the model varies from latitude 40°S to 60°S across these 13 sites at both the PI and LGM. Note that the transport estimation is quite sensitive to using a different latitude for the Coriolis parameter. Nevertheless, the midpoint 50°S generally gives a more accurate estimate of baroclinic transport with the smallest percent error (0.0988 and 0.0793 for the PI and LGM, respectively), except the Drake Passage site where the difference is relatively small due to its narrow channel. Particularly at the AU sector, using the Coriolis parameter at the midpoint 50°S produces the best match between the estimated and true baroclinic transport. The following estimates of ACC baroclinic transport thus use a latitude of 50°S to calculate the Coriolis parameter.

5. Reconstructing Baroclinic Transport Using End-Member Water Masses

We now test methods of Step 2 (S2), which further assumes that the density observation is limited to only a few end-member water masses at the northern margin of the ACC. As such, the vertical density profile needs to be reconstructed from water properties of the end-member water masses and the vertical profile of $\delta^{18}O_c$. We first discuss the most ideal case (S2_M1) where the temperature and salinity of three end-member water masses (STSW, AAIW, and LCDW) at northern margin are available for both time intervals and are then weighted by the $\delta^{18}O_c$ profile. The reconstructed temperature and salinity profiles, in turn, are used to calculate the north margin density profile. The $\delta^{18}O_c$ profile here is calculated from model seawater $\delta^{18}O_{sw}$ and temperature in °C (Marchitto et al., 2014)

$$\delta^{18}O_c = \delta^{18}O_{sw} - 0.27 + 0.0011T^2 - 0.245T + 3.58 \tag{5}$$

which is in good agreement with the data from LS16 (Figure S3 in Supporting Information S1). The weighted fraction (f_w) between STSW and AAIW or between AAIW and LCDW in S2 are calculated as follows

$$\begin{aligned} f_{w,\mathrm{STSW-AAIW}} &= \left(\delta^{18}O_{c,\mathrm{AAIW}} - \delta^{18}O_c\right) / \left(\delta^{18}O_{c,\mathrm{AAIW}} - \delta^{18}O_{c,\mathrm{STSW}}\right) \\ f_{w,\mathrm{AAIW-LCDW}} &= \left(\delta^{18}O_{c,\mathrm{LCDW}} - \delta^{18}O_c\right) / \left(\delta^{18}O_{c,\mathrm{LCDW}} - \delta^{18}O_{c,\mathrm{AAIW}}\right) \end{aligned} \tag{6}$$

The temperature T and salinity S profiles thus can be calculated with the weight of fraction f_w as

$$\begin{aligned} T_{\mathrm{STSW-AAIW}} &= f_{w,\mathrm{STSW-AAIW}} \times T_{\mathrm{STSW}} + \left(1 - f_{w,\mathrm{STSW-AAIW}}\right) \times T_{\mathrm{AAIW}} \\ T_{\mathrm{AAIW-LCDW}} &= f_{w,\mathrm{AAIW-LCDW}} \times T_{\mathrm{AAIW}} + \left(1 - f_{w,\mathrm{AAIW-LCDW}}\right) \times T_{\mathrm{LCDW}} \\ S_{\mathrm{STSW-AAIW}} &= f_{w,\mathrm{STSW-AAIW}} \times S_{\mathrm{STSW}} + \left(1 - f_{w,\mathrm{STSW-AAIW}}\right) \times S_{\mathrm{AAIW}} \\ S_{\mathrm{AAIW-LCDW}} &= f_{w,\mathrm{AAIW-LCDW}} \times S_{\mathrm{AAIW}} + \left(1 - f_{w,\mathrm{AAIW-LCDW}}\right) \times S_{\mathrm{LCDW}} \end{aligned} \tag{7}$$

In the ideal case S2_M1, the northern margin density profile can be reconstructed from end-member water masses. Nevertheless, the density stratification can be underestimated. Figure 5 shows $\delta^{18}O_{sw}$-S-T relationship in observations and iCESM PI and LGM simulations. Although there are some biases in PI simulation (more depleted seawater $\delta^{18}O_{sw}$ at AU section), the model $\delta^{18}O_{sw}$-S-T during the PI supports the observations of LS16 such that the modern $\delta^{18}O_{sw}$-S-T relationship can be approximated as a linear mixing relation between pairs of the three end-member water masses (Figures 5a–5e). However, the model $\delta^{18}O_{sw}$-S diagram during the LGM (Figure 5f) shows a linear mixing between STSW and AAIW, but changes to a nonlinear mixing between AAIW and LCDW. More importantly, at both time intervals, the reconstructed T-S diagrams between pairs of three end-member water masses tend to be straight lines, while the model T-S diagrams are quite curved (Figures 5b and 5c). This discrepancy between the model and reconstructed T-S diagrams is mostly due to the reconstruction methodology and suggests that the density profile reconstruction may be inaccurate. A closer look at reconstructed property profiles (Figures 6a–6c) suggests that the density gradient can be underestimated. As shown in Figure 6a, the temperature profile can be accurately reconstructed at both the PI and LGM (see Appendix A for details). Nevertheless, in Figure 6b, the reconstructed salinity is much saltier than the model salinity below the AAIW depth (up to 0.2 psu for the PI and 0.5 psu for the LGM), which leads to relatively high reconstructed density (Figure 6c). This higher reconstructed density thus can result in an underestimation of the density gradient. As such, compared to S1_M2, the transport estimation in S2_M1 is reduced by 28.5% and 60.0% at the PI and LGM, respectively (Table 2).

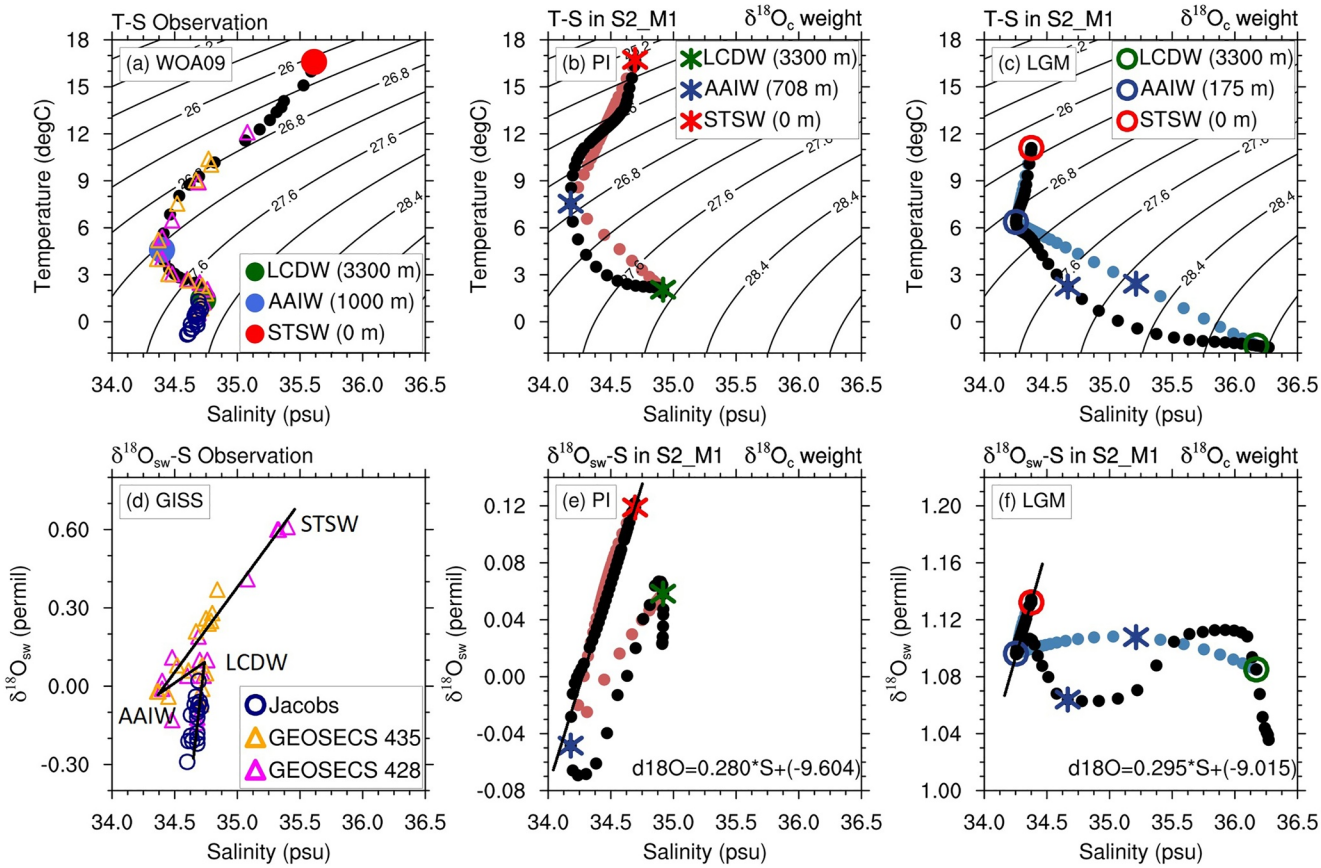

Figure 5. The T-S (top panels) and $\delta^{18}O_{sw}$-S (bottom panels) diagrams in the observations and in the isotope-enabled Community Earth System Model pre-industrial and Last Glacial Maximum (LGM) simulations. T and S for Australia margin from WOA09 in (a). S and $\delta^{18}O_{sw}$ from GEOSECS stations and along the Antarctic Margin (Jacobs et al., 2005; Schmidt et al., 1999) in (d). Black dots are from the model and colored dots are from reconstruction S2_M1 in (b, c, e, and f). Contours indicate isopycnals (contour interval = 0.4 kg m^{-3}). Markers (solid circle, asterisk, and open circle) are end-member water masses Subtropical Surface Water (STSW) (red), Antarctic Intermediate Water (AAIW) (blue), and Lower Circumpolar Deep Water (green). Black lines in (e and f) show the regression lines for black dots between STSW and AAIW.

It should also be noted that the model AAIW depth at LGM is substantially shallower than that at the PI. This suggests that keeping the LGM AAIW depth the same as PI AAIW depth may result in a large error in the reconstructed LGM salinity profile especially between STSW and AAIW, leading to an inaccurate reconstructed density profile and ACC transport. The model T-S diagrams show that the AAIW depth is about 708 m at the PI (Figure 5b), whereas the AAIW depth shallows to 175 m at the LGM (Figure 5c). A further examination demonstrates that the shallower AAIW depth during the LGM is probably due to the northward movement of AAIW. Figure 7 shows meridional sections of zonal mean salinity at the PI and LGM and marks the location of sea surface salinity (SSS) minimum. The tongue of low salinity AAIW shallows at the LGM compared with that at the PI, and the SSS minimum in the SO changes from south to north during the LGM, suggesting a northward movement of AAIW. Note that this shift seems to be systematic, not only in the iCESM (Figure 7), but also in PMIP3 models (Figure S4 in Supporting Information S1). This northward movement of AAIW implies that the AAIW depth could have been shallower during the LGM at the AU sector. The physical mechanism for this systematic shift and shoaling of AAIW at LGM is presented in a separate work (Li et al., 2021).

Given the underestimated density gradient in S2_M1, we explore the case S2_M2 if the estimation can be improved with one additional pore fluid observation obtained below the AAIW depth. Our result shows that, in this case S2_M2, the transport estimation can indeed be substantially improved. Figure 8 shows the reconstructed $\delta^{18}O_{sw}$-S-T diagrams in S2_M2 with one more pore fluid observation at ~1 km assumed available in the reconstruction. The reconstructed T-S diagrams now compare much better with the model

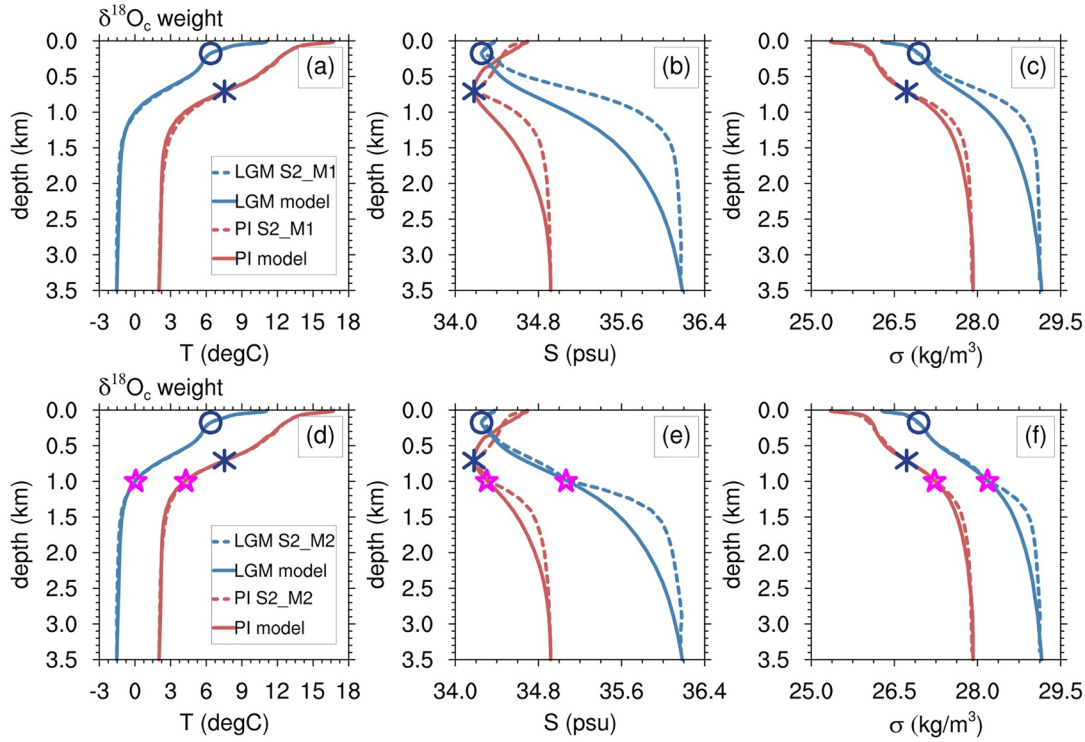

Figure 6. The model (solid lines) and reconstructed (dashed lines) temperature, salinity, and potential density profiles at the pre-industrial (PI) (red) and Last Glacial Maximum (LGM) (blue) in the reconstruction S2_M1 (tope panel) and S2_M2 (bottom panel). Blue asterisk markers correspond the Antarctic Intermediate Water (AAIW) depth at the PI; open circles correspond the AAIW depth at the LGM; and magenta open stars correspond the depth of additional pore fluid observation at ~1 km added in S2_M2.

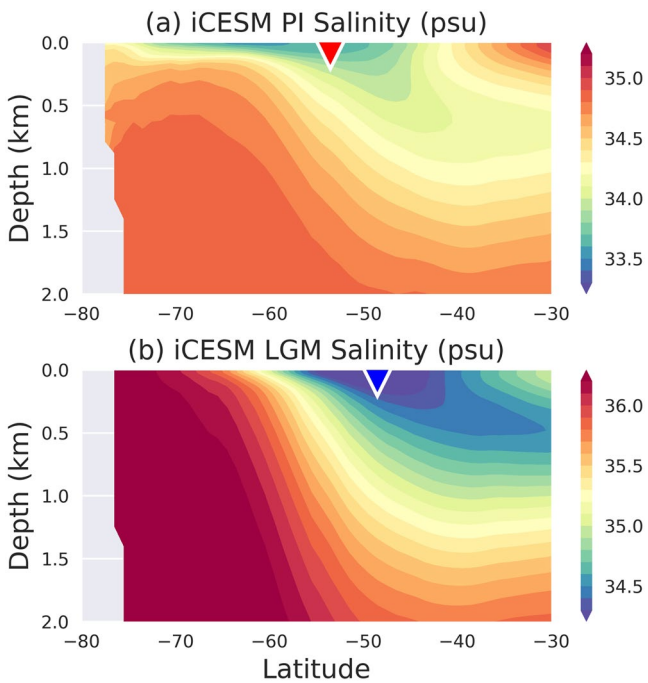

Figure 7. Zonal mean salinity in color shading at the pre-industrial (PI) and Last Glacial Maximum (LGM). Triangle markers correspond to the locations of sea surface salinity minimum at the PI (red) and LGM (blue).

T-S diagrams at both the LGM and PI (Figures 8a and 8b). More specifically, as the temperature profiles can be reconstructed accurately in both S2_M1 and S2_M2 (Figures 6a and 6d), the reconstructed salinity profile is much closer to the model salinity profile below the AAIW depth in S2_M2 (Figure 6e) than in S2_M1 (Figure 6b). Consequently, the reconstructed density profiles are relatively closer in the S2_M2 to the S2_M1 (Figures 6c and 6f). This improved reconstructed density profile hence results in the transport estimations in S2_M2 reduced by 17.9% and 38.6% respectively (Table 2). In short, the study in this section suggests that the ACC baroclinic transport can potentially be reconstructed from end-member water masses alone. Furthermore, the estimation can be greatly improved by one additional site for pore fluid based on T and S estimates obtained below the AAIW depth in the reconstruction.

6. Reconstructing Baroclinic Transport Using Reconstructed End-Member Water Masses

6.1. Method for Reconstructing STSW and AAIW Paleosalinities

As the density profile can be reconstructed from end-member water masses alone, we finally test the method of Step 3 (S3), which further relaxes the observational condition such that paleo-salinities of end-members STSW and AAIW need to be reconstructed independently. In LS16, the paleo-salinities of end-member water masses are reconstructed through the linear $\delta^{18}O_{sw}$-S relationship of surface and intermediate waters in the South Indian Ocean. It assumes that this $\delta^{18}O_{sw}$-S relationship of the

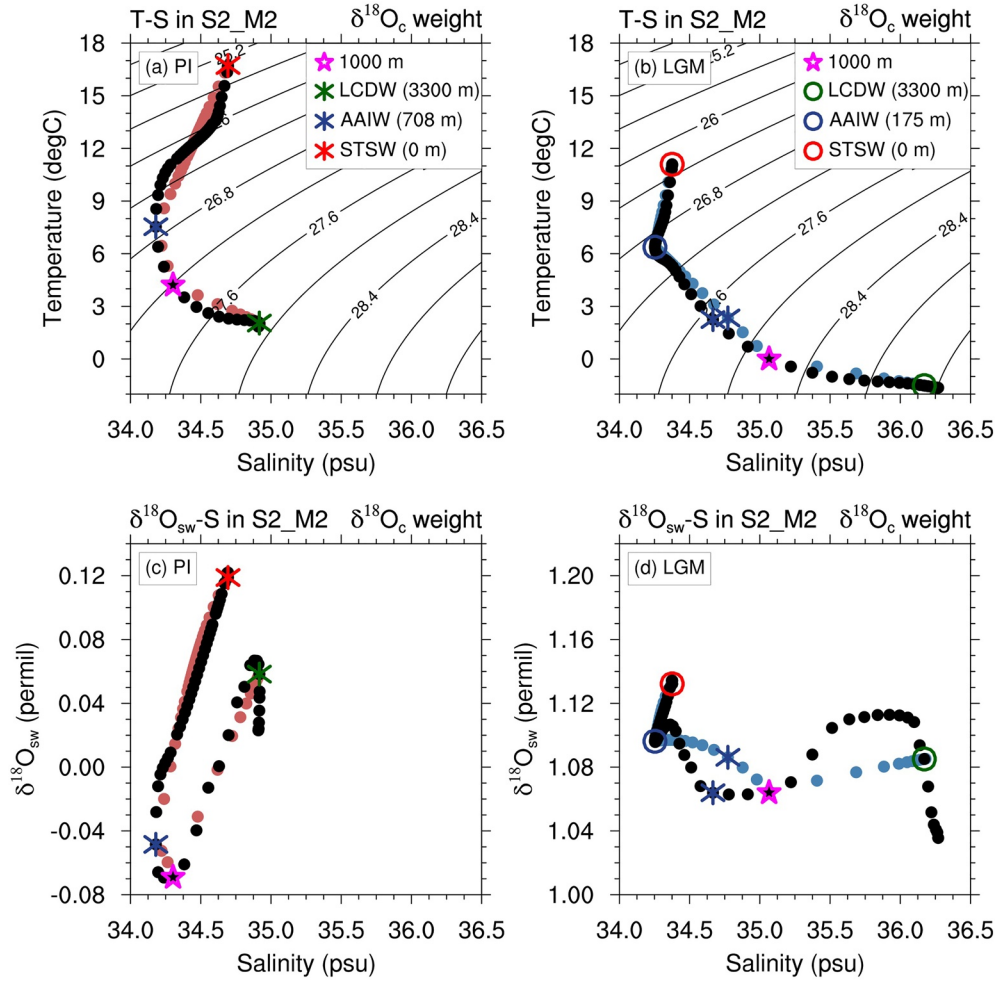

Figure 8. The T-S (top panels) and $\delta^{18}O_{sw}$-S (bottom panels) diagrams in the isotope-enabled Community Earth System Model for the reconstruction S2_M2 with one additional water mass at ~1 km. Magenta open stars correspond to the one additional water mass added in the S2_M2.

present day, the result of mixing between subtropical gyre waters and high-latitude freshwater end-member, holds during the LGM

$$\delta^{18}O_{sw} = \left[\left(\delta^{18}O_{fresh} - \delta^{18}O_{gyre}\right) / \left(S_{fresh} - S_{gyre}\right)\right] \times S + \delta^{18}O_{fresh} \quad (8)$$

where $\delta^{18}O_{fresh}$ is the $\delta^{18}O$ of freshwater end-member; $\delta^{18}O_{gyre}$ is the $\delta^{18}O$ of subtropical gyre; S_{fresh} is the salinity of freshwater end-member (typically ~0); and S_{gyre} is the salinity of subtropical gyre. More importantly, it also assumes that this linear $\delta^{18}O_{sw}$-S relationship in the South Indian Ocean can reproduce well the $\delta^{18}O_{sw}$-S relationship between the STSW and AAIW at the AU section. Therefore, the salinity of STSW and AAIW can be estimated as

$$S = \left(\delta^{18}O_{sw} - \delta^{18}O_{fresh}\right) \times \left[-S_{gyre} / \left(\delta^{18}O_{fresh} - \delta^{18}O_{gyre}\right)\right] \quad (9)$$

where S_{gyre} can be estimated from observations in the South Indian Ocean; $\delta^{18}O_{gyre}$ and $\delta^{18}O_{fresh}$ can be inferred from observationally derived Equation 8; and the $\delta^{18}O_{sw}$ of STSW and AAIW can be calculated from Equation 5 with $\delta^{18}O_c$ and T observations for the end-member water masses. As such, the LGM salinity of end-member water masses (STSW and AAIW) can be reconstructed if the LGM S_{gyre}, $\delta^{18}O_{gyre}$, $\delta^{18}O_{fresh}$, and $\delta^{18}O_{sw}$ of end-member water masses are given independently.

More specifically, in LS16, the LGM $\delta^{18}O_{sw}$ of STSW and AAIW are estimated from Equation 5 given the independent measurements of LGM $\delta^{18}O_c$ and T. Since the real-world $\delta^{18}O_{sw}$-S relationship is unknown at

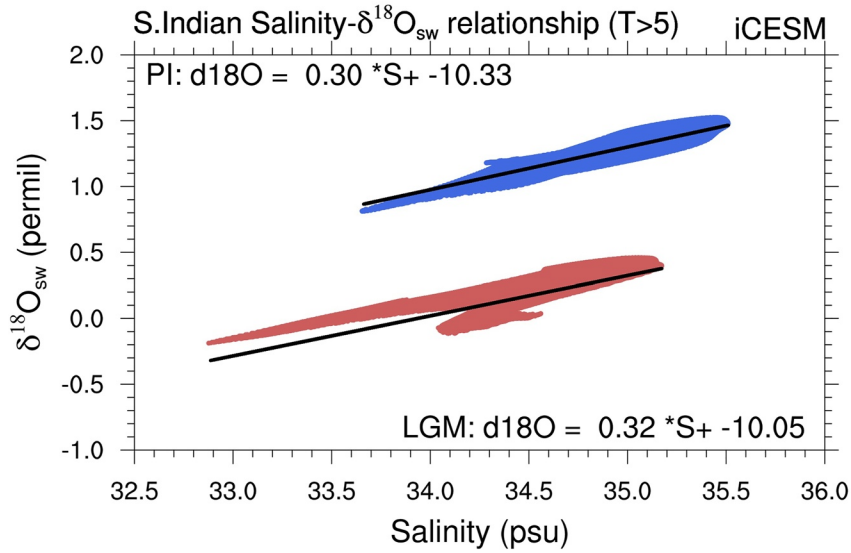

Figure 9. The $\delta^{18}O_{sw}$-S relationship of surface and intermediate waters in the South Indian Ocean at the pre-industrial (red dots) and Last Glacial Maximum (blue dots). Black lines show the regression lines for the red and blue dots, respectively.

LGM, the change of subtropical gyre end-members ($\delta^{18}O_{gyre}$ and S_{gyre}) are estimated from the whole ocean $\delta^{18}O_{sw}$ and salinity difference between the PI and the LGM, and the LGM $\delta^{18}O_{fresh}$ can be inferred from modeling studies, as supported by the observations of precipitation $\delta^{18}O_p$. Largely following the LS16, we first reconstruct the salinities of STSW and AAIW in S3_M1. The model $\delta^{18}O_{sw}$ of the end-members are directly used in our test method S3_M1 for the PI and LGM. The PI subtropical gyre end-member S_{gyre} is estimated in the South Indian Ocean, and then $\delta^{18}O_{gyre}$ is estimated given the model $\delta^{18}O_{sw}$-S relationship Equation 8 in the South Indian Ocean. Since the LGM $\delta^{18}O_{sw}$-S relationship is assumed to be unknown, the PI subtropical gyre end-members (S_{gyre} and $\delta^{18}O_{gyre}$) thus are increased by the global mean difference (1.11 psu and 1.03‰, respectively) for the LGM. The PI $\delta^{18}O_{fresh}$ can be inferred from the $\delta^{18}O_{sw}$-S relationship in the South Indian Ocean, but the LGM $\delta^{18}O_{fresh}$ is approximated from local precipitation $\delta^{18}O_p$ difference. Note that since the iCESM is a fully coupled model, $\delta^{18}O$ outputs from the atmosphere and ocean components are self-consistent. As salinities of end-member water masses are reconstructed, the density profile will then be reconstructed (denoted as S3_M1) same as the method S2_M1.

6.2. Reconstructing Paleosalinities of STSW and AAIW in the iCESM

In the iCESM, results of S3_M1 show that the paleosalinity of STSW and AAIW can be further reconstructed based on the linear $\delta^{18}O_{sw}$-S mixing relationship in the South Indian Ocean. The model $\delta^{18}O_{sw}$-S mixing relationships between STSW and AAIW at the AU sector are found linear at both the PI and the LGM, and the LGM slope (~0.295‰/psu) is close to the PI slope (~0.280‰/psu) (Figures 5c and 5d). These linear mixing relationships confirm the assumption that the $\delta^{18}O_{sw}$-S-T relationship can be approximated as a linear mixing relation between STSW and AAIW at both time intervals. Furthermore, the linear $\delta^{18}O_{sw}$-S relation between STSW and AAIW at AU sector can be reproduced well in the South Indian Ocean in the iCESM. Figure 9 shows the $\delta^{18}O_{sw}$-S relation of surface and intermediate waters in the South Indian Ocean at the LGM, which are offset from the PI because global salinity and seawater $\delta^{18}O_{sw}$ increase by about 1‰ respectively at the LGM due to land ice expansion. However, the regression lines are linear at both the PI and the LGM, with the LGM slope (~0.32‰/psu) similar to the PI slope (~0.30‰/psu). This implies that the linear $\delta^{18}O_{sw}$-S mixing relation in the South Indian Ocean can be used to reconstruct the salinities of end-member water masses STSW and AAIW.

Physically, the freshwater end-member needs to be inferred from the linear $\delta^{18}O_{sw}$-S mixing relation in Equation 8, in order to reconstruct the salinities of STSW and AAIW. In this case, the PI freshwater end-member is shown to be about −10.33‰ from the $\delta^{18}O_{sw}$-S relation in the South Indian Ocean (Figure 9), which is

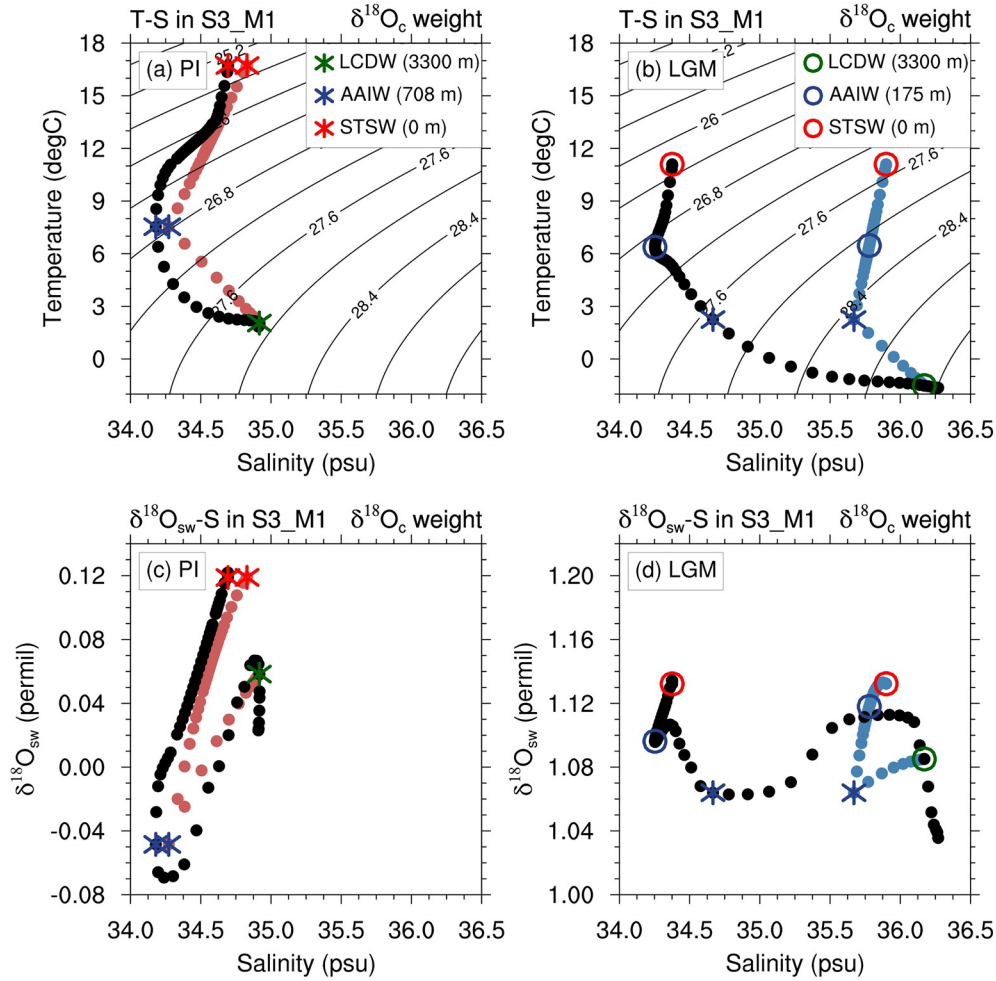

Figure 10. The model and reconstructed T-S (top panel) and $\delta^{18}O_{sw}$-S (bottom panel) diagrams at the pre-industrial (PI) and Last Glacial Maximum (LGM). Black dots are from the model; colored dots are from the reconstruction S3_M1 where salinities of Subtropical Surface Water (STSW) and Antarctic Intermediate Water (AAIW) are reconstructed independently. Contours indicate isopycnals (contour interval = 0.4 kg m^{-3}). Markers are end-member water masses STSW (red), AAIW (blue), and Lower Circumpolar Deep Water (LCDW) (green) for the PI (asterisk) and LGM (open circle). The uncertainties in reconstructed LGM temperature for STSW, AAIW, and LCDW are ±1°C, ±1°C, and ±0.25°C, respectively. The uncertainties in reconstructed LGM salinity for STSW, AAIW, and LCDW are ±0.87 psu, ±0.93 psu, and ±0.035 psu, respectively. The uncertainties in reconstructed LGM $\delta^{18}O_{sw}$ for STSW, AAIW, and LCDW are ±0.23‰, ±0.25‰, and ±0.05‰, respectively.

similar to the model value of freshwater end-member (−9.60‰) derived from the linear $\delta^{18}O_{sw}$-S relation between the STSW and AAIW at the AU sector (Figure 5e). However, the LGM freshwater end-member are shown to be enriched slightly in the iCESM (Figures 5f and 9), instead of more depleted as suggested in LS16. The enrichment of the LGM freshwater end-member is also consistent with the approximation method in S3_M1 from the model local precipitation $\delta^{18}O_p$ difference in the South Indian Ocean, which is enriched about 0.77‰ during the LGM. As such, the LGM $\delta^{18}O_{sw}$-S relationship is derived as $\delta^{18}O_{sw} = 0.298 \times S\text{-}9.56$, and salinities of STSW and AAIW at LGM are reconstructed in Equation 8.

6.3. Transport Reconstruction and Monte Carlo Estimate

With the salinity of end-member water masses reconstructed based on the $\delta^{18}O_{sw}$-S relationship, the density profile is reconstructed in the case S3_M1. Our result shows that the transport estimation in S3_M1 is reduced by 32.2% and 77.9% at the PI and LGM, respectively (Table 2). As shown in Figure 10a, the reconstructed T-S diagram is relatively close to the modeled T-S diagram during the PI. This suggests that

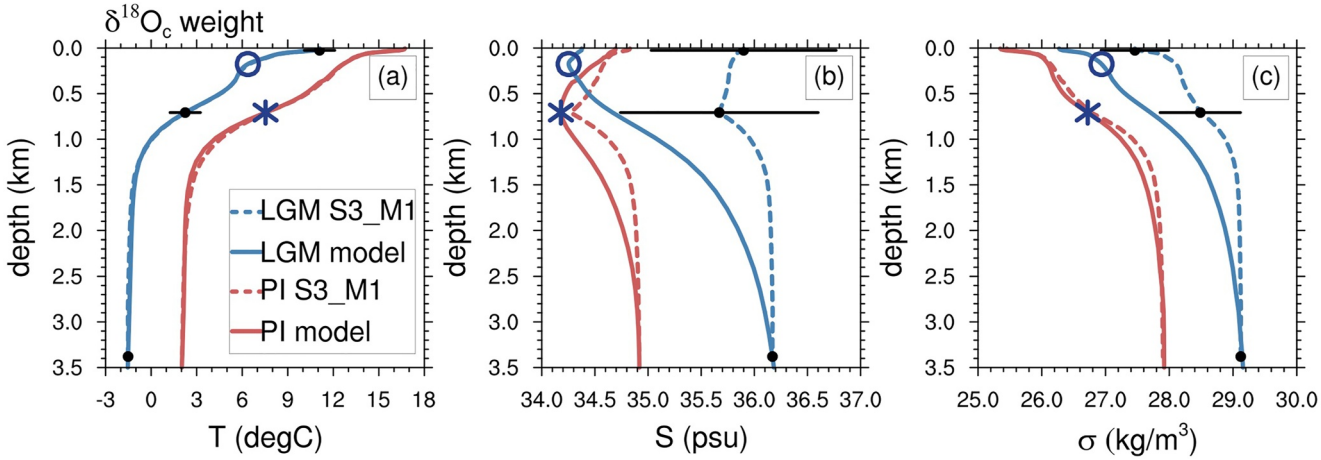

Figure 11. The model (solid lines) and reconstructed (dashed lines) (a) temperature, (b) salinity, and (c) potential density profiles at the Australia (135°E) sector during the pre-industrial (red) and Last Glacial Maximum (LGM) (blue) for the reconstruction S3_M1. The uncertainties (black lines) in reconstructed LGM potential density for Subtropical Surface Water, Antarctic Intermediate Water, and Lower Circumpolar Deep Water are ±0.53, ±0.63, and ±0.03 kg/m^3, respectively.

the reconstruction method S3_M1 is plausible such that the salinities of end-member water masses and the density profile in S3_M1 can be reconstructed reasonably well. However, during the LGM, the reconstructed T-S diagram is substantially distinct from the model T-S diagram (Figure 10b). The reconstructed $\delta^{18}O_{sw}$-S relationship between pairs of the end-member water masses is also close to the model for the PI (Figure 10c), but the relationship changes dramatically for the LGM (Figure 10d). A closer examination of the reconstructed temperature and salinity profiles also indicates that both the temperature and salinity profiles can be reconstructed reasonably well during the PI (Figures 11a and 11b). However, the reconstructed salinity during the LGM is much saltier (up to 1.5 psu) than the model (Figure 11b). Therefore, the reconstructed LGM density is higher than the model (Figure 11c), resulting in an underestimate of the density gradient and large reduction in the transport estimate. The overestimated paleosalinity of STSW and AAIW is mostly due to the freshwater end-member estimate, which is challenging to accurately approximate in S3_M1. The transport estimate in S3_M1 suggests that the paleosalinities of end-member water masses can be reconstructed from the linear $\delta^{18}O_{sw}$-S mixing relationship in the South Indian Ocean. However, an accurate estimate of the LGM $\delta^{18}O_{fresh}$ in the S3_M1 needs further exploration.

In order to assess whether reconstructed end-member water mass properties and transport are significantly different from the model, we perform Monte Carlo experiment in the method S3_M1, given the estimated uncertainty of each input parameter. Although actual values of input parameters in S3_M1 are extracted from iCESM, the uncertainties on each parameter are estimated based on LS16. As such, the uncertainty in the $\delta^{18}O_c$ profile is about ±0.07‰ (LS16). The uncertainty in $\delta^{18}O_c$ profile (±0.07‰) incorporates analytical uncertainty, proxy uncertainty, and age model uncertainty, and is estimated from the difference between the Holocene benthic foraminiferal values and predicted values based on the modern water column data in LS16. The uncertainties in the temperature and salinity of LCDW are taken from Adkins et al. (2002). There are suggestions that the errors on the pore water reconstruction may be underestimated (Miller et al., 2015; Wunsch, 2016a, 2016b). These uncertainties and its implications may in turn result in larger transport error and need to be considered in a real-world paleo-application.

For the temperatures of STSW and AAIW, we assign a 1-sigma error of ±1°C. Moreover, we assign a relatively large error estimate of ±1‰ on the freshwater end-member ($\delta^{18}O_{fresh}$), and ±0.1‰ and ±0.137 psu on the subtropical gyre $\delta^{18}O_{gyre}$ and S_{gyre} respectively. The uncertainties on latitude and AAIW depth also keep consistent with LS16, which are assigned 1-sigma uncertainties of ±2.5° and ±100 m, respectively.

The Monte Carlo estimate shows that the method S3_M1 yields a 1-sigma uncertainty of ±35.3 Sv for LGM ACC transport reconstruction (Table 2), allowing for a wide range in LGM ACC transport. This total error on the transport calculation is contributed mostly due to the uncertainties in AAIW temperature, such that the transport error can be reduced by 44.1% if the uncertainty in AAIW temperature is zero. If the error can

be thus reduced, the relative sizes of the PI and LGM estimates would become significantly different. The assumed $\delta^{18}O_{gyre}$ and S_{gyre} used in Equation 9 to estimate salinities for STSW and AAIW could also contribute to the transport error, which can be reduced by 12.8% if uncertainties in $\delta^{18}O_{gyre}$ and S_{gyre} are zero. The Monte Carlo test shows that 1-sigma uncertainties in reconstructed LGM salinities for STSW and AAIW are about ±0.87 psu and ±0.93 psu, respectively (Figure S7 in Supporting Information S1). Thus, reconstructed densities for STSW and AAIW and transport reconstruction are significantly different from the model values (Figure 11c).

7. Conclusions

In this work, we test systematically a series of methods for reconstructing the glacial ACC baroclinic transport in the context of an isotope-enabled coupled climate model iCESM. This series of methods are staggered in three steps with increased degree of approximation to meet the presumably increased restrictions toward realistic paleo-observation scenarios. We find that the ACC baroclinic transport can be reconstructed from end-member water masses (STSW, AAIW, and LCDW) and the vertical profile of $\delta^{18}O_c$ at the Australian margin. The model results also show that adding more direct information from pore fluid observations at intermediate depths may allow better transport reconstruction. But the uncertainties of pore-water reconstructions and its implications for transport reconstruction need to be considered in the real-world reconstructions (Wunsch, 2016a, 2016b). Moreover, as the observational condition is further relaxed that density is only available for LCDW, paleosalinities of STSW and AAIW can be reconstructed independently from the $\delta^{18}O_{sw}$-S relationship of surface and intermediate waters in the South Indian Ocean. However, the uncertainties in the reconstructed paleosalinity of end-members are exceedingly large, leading to a hugely reduced transport estimation with large error. This suggests that caution should be taken when reconstructing paleosalinities of end-member water masses due to the challenge to accurately estimate the paleo freshwater end-member, which needs further exploration.

This work reinforces the conclusion reached in LS16 that without better constraints on LGM salinity, the error in the estimate of ACC transport based primarily on $\delta^{18}O_{sw}$ are unacceptably large. However, our study shows that a modest number of pore water salinity reconstructions on the northern margin of the ACC, interpolated using $\delta^{18}O_c$ measurements at higher vertical resolution, is a viable approach. Adding direct information about temperature and salinity from pore water reconstructions south of the ACC could further constrain LGM ACC transport.

Both models and reconstructions are subject to substantial biases and uncertainties. The bottom topography and eddies are essential in the dynamics of the ACC and associated transport. The relatively coarse-resolution model used in this work could potentially cause problems because of the lack of eddy fluxes and relatively coarse bottom topography. Additionally, the model simulates relatively fresher surface water compared with observations. These biases could influence findings on reconstructing paleosalinities of end-member water masses and associated ACC transport. However, our work focuses on the methodology, in principle, necessary to reconstruct glacial ACC baroclinic transport and on the associated assumptions in LS16, using the model as a substitute to the real world. In the future, it would be highly desirable to perform similar tests in models at higher (eddy permitting or resolving) resolution and simulations for future changes.

Appendix A: Role of Weight Profile on Reconstructing Density Profile

Observations of $\delta^{18}O_c$ are often used as weight profile in the reconstruction methods because it is one of the most abundant proxy observations and can be easily acquired at the Australia section. Interestingly, even in the most ideal case S2_M1 (Section 5) that the density observation is limited to end-member water masses (STSW, AAIW, and LCDW) on the northern side, the reconstructed density gradient tends to be underestimated and the transport estimation is reduced by 28.6% and 60% for the PI and LGM, respectively. Therefore, we assess the role of weight profile on the reconstruction method here by having several property profiles ($\delta^{18}O_{sw}$, salinity, temperature, and potential density) as weight. The weight fraction f_w is calculated the same as $\delta^{18}O_c$ in Equation 6 and the density profile is then reconstructed same as the method S2_M1.

In this case that different property profiles are used as weight, the $\delta^{18}O_c$ profile can reconstruct the temperature and salinity reasonably well. Figure A1 shows the model and reconstructed temperature, salinity, and potential density profiles in S2_M1 weighted by different property profiles. The temperature and salinity profiles cannot be reconstructed well during the LGM (Figures A1a–A1c) when $\delta^{18}O_{sw}$ is used as weight profile. This is because the $\delta^{18}O_{sw}$ is no longer linearly related with salinity between the AAIW and LCDW at LGM (Figure 5d). The reconstructed profiles (Figures A1d–A1f) weighted by the temperature are similar to that weighted by the $\delta^{18}O_c$ (Figures 6a–6c). This is because, at both the PI and LGM, temperature and $\delta^{18}O_c$ profiles are monotonically decreasing and increasing, respectively. As such, the $\delta^{18}O_c$ can be linearly related to the temperature. Moreover, the reconstructed density gradient tends to be overestimated when salinity is used as weight profile (Figures A1g–A1i), and the reconstructed density is the most ideal case when density is used as weight (Figures A1j–A1l). This suggests that practically the $\delta^{18}O_c$ profile can be used to weight the contribution of end-member water masses to reconstruct the temperature and salinity profiles reasonably well as it is linearly related to the temperature. Furthermore, the reconstructed T-S diagrams in this case always show straight lines between pairs of the end-member water masses due to the reconstruction methodology (Figures S5 and S6 in Supporting Information S1). This indicates that the density profile reconstruction may be inaccurate no matter which weight profile is used in the reconstruction, and this can be improved by adding one pore fluid observation below the AAIW depth discussed in Section 5.

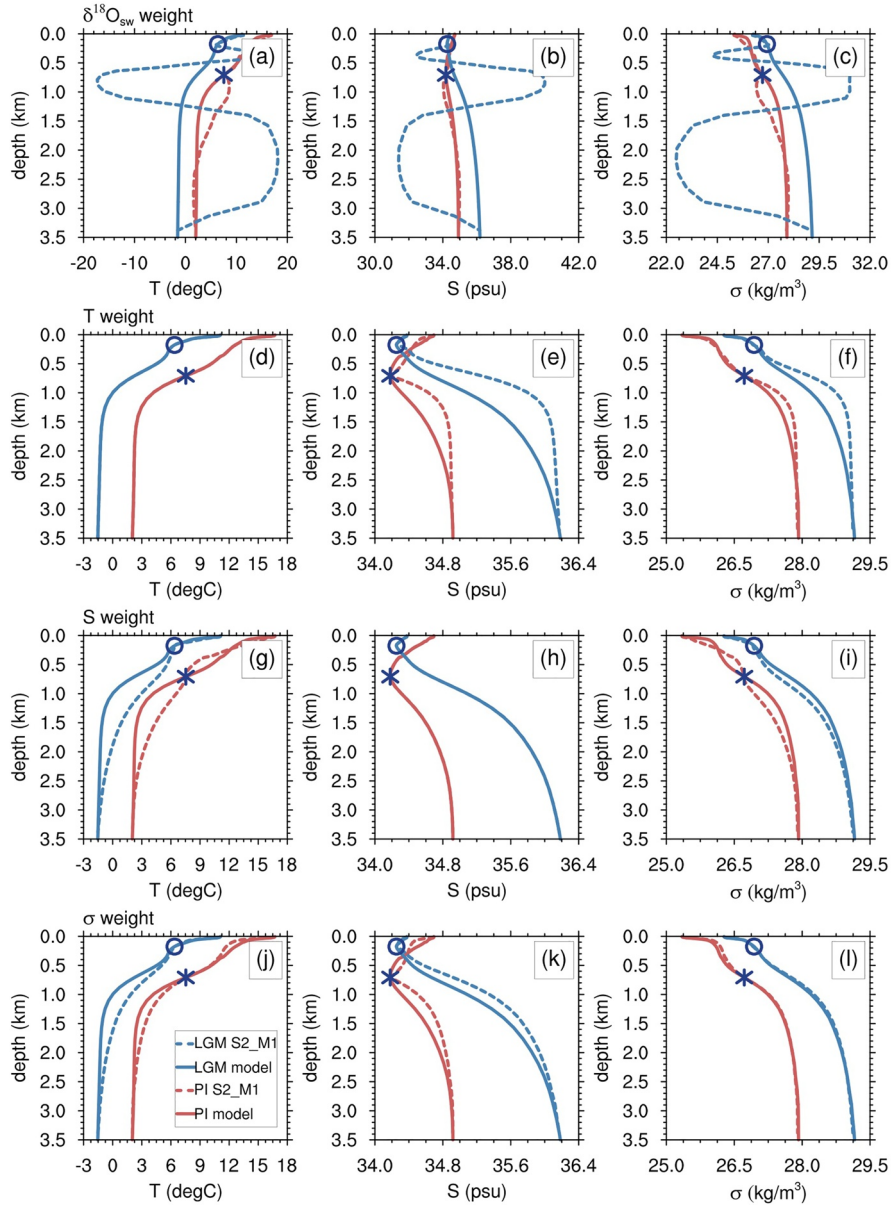

Figure A1. The model (solid lines) and reconstructed (dashed lines) temperature, salinity, and potential density profiles at the PI (red) and Last Glacial Maximum (LGM) (blue) in the S2_M1 using different weight profiles. Markers correspond to the Antarctic Intermediate Water depth at the PI (blue asterisk) and LGM (open circle).

Data Availability Statement

Computing and data storage resources, including the Cheyenne supercomputer (https://doi.org/10.5065/D6RX99HX), were provided by the Computational and Information Systems Laboratory (CISL) at NCAR. iCESM output supporting our findings is available at https://doi.org/10.26024/b290-an76. Required PMIP3 model outputs were accessed and downloaded from the PMIP3 server (under the Project module on the left side of the webpage at https://esgf-node.llnl.gov/search/cmip5/). Required WOA09 data were downloaded from https://www.nodc.noaa.gov/OC5/WOA09/woa09data.html. Required seawater oxygen-18 data were downloaded from https://data.giss.nasa.gov/o18data/.

Acknowledgments
This work is supported by US National Science Foundation NSF OCE-1810681. The CESM project is supported primarily by the NSF. This material is based on work supported by the National Center for Atmospheric Research, which is a major facility sponsored by the NSF under Cooperative Agreement no. 1852977. We also acknowledge the World Climate Research Programme's Working Group on Coupled Modeling, and we thank the climate modeling groups (listed in Table 1) for producing and making available their model output, the Earth System Grid Federation (ESGF) for archiving the data and providing access, and the multiple funding agencies who support CMIP, PMIP, and ESGF.

References

Adkins, J. F., Mclntyre, K., & Schrag, D. P. (2002). The salinity, temperature, and $\delta^{18}O$ of the glacial deep ocean. *Science*, *298*(5599), 1769–1773. https://doi.org/10.1126/science.1076252

Antonov, J. I., Seidov, D., Boyer, T. P., Locarnini, R. A., Mishonov, A. V., Garcia, H. E., et al. (2010). *World Ocean Atlas 2009, volume 2: Salinity (S. Levitus)*. NOAA Atlas NESDIS 69, U.S. Government Printing Office.

Braconnot, P., Harrison, S. P., Kageyama, M., Bartlein, P. J., Masson-Delmotte, V., Abe-Ouchi, A., et al. (2012). Evaluation of climate models using palaeoclimatic data. *Nature Climate Change*, *2*(6), 417–424. https://doi.org/10.1038/nclimate1456

Braconnot, P., Otto-Bliesner, B., Harrison, S., Joussaume, S., Peterchmitt, J.-Y., Abe-Ouchi, A., et al. (2007). Results of PMIP2 coupled simulations of the Mid-Holocene and Last Glacial Maximum—Part 2: Feedbacks with emphasis on the location of the ITCZ and mid- and high latitudes heat budget. *Climate of the Past*, *3*(2), 279–296. https://doi.org/10.5194/cp-3-279-2007

Brady, E., Stevenson, S., Bailey, D., Liu, Z., Noone, D., Nusbaumer, J., et al. (2019). The connected isotopic water cycle in the Community Earth System Model Version 1. *Journal of Advances in Modeling Earth Systems*, *11*(8), 2547–2566. https://doi.org/10.1029/2019MS001663

Brennan, C. E., Meissner, K. J., Eby, M., Hillaire-Marcel, C., & Weaver, A. J. (2013). Impact of sea ice variability on the oxygen isotope content of seawater under glacial and interglacial conditions. *Paleoceanography*, *28*(3), 388–400. https://doi.org/10.1002/palo.20036

Burke, A., & Robinson, L. F. (2012). The southern ocean's role in carbon exchange during the last deglaciation. *Science*, *335*(6068), 557–561. https://doi.org/10.1126/science.1208163

Clark, P. U., Dyke, A. S., Shakun, J. D., Carlson, A. E., Clark, J., Wohlfarth, B., et al. (2009). The Last Glacial Maximum. *Science*, *325*(5941), 710–714. https://doi.org/10.1126/science.1172873

Craig, H., Gordon, L. I., & Tongiori, E. (1965). Deuterium and oxygen 18 variations in the ocean and the marine atmosphere. In *Stable isotopes in oceanographic studies and paleotemperatures* (pp. 9–130). Proceedings of the Third Spoleto Conference.

Cunningham, S. A., Alderson, S. G., King, B. A., & Brandon, M. A. (2003). Transport and variability of the Antarctic Circumpolar Current in Drake Passage. *Journal of Geophysical Research*, *108*(C5), 8084. https://doi.org/10.1029/2001JC001147

Farneti, R., Delworth, T. L., Rosati, A. J., Griffies, S. M., & Zeng, F. (2010). The role of mesoscale eddies in the rectification of the Southern Ocean response to climate change. *Journal of Physical Oceanography*, *40*(7), 1539–1557. https://doi.org/10.1175/2010JPO4353.1

Gent, P. R., Danabasoglu, G., Donner, L. J., Holland, M. M., Hunke, E. C., Jayne, S. R., et al. (2011). The Community Climate System Model Version 4. *Journal of Climate*, *24*(19), 4973–4991. https://doi.org/10.1175/2011JCLI4083.1

Gnanadesikan, A., & Hallberg, R. W. (2000). On the relationship of the circumpolar current to Southern Hemisphere winds in coarse-resolution ocean models. *Journal of Physical Oceanography*, *30*, 22. https://doi.org/10.1175/1520-0485(2000)030<2013:otrotc>2.0.co;2

Gu, S., Liu, Z., Lynch-Stieglitz, J., Jahn, A., Zhang, J., Lindsay, K., & Wu, L. (2019). Assessing the ability of zonal $\delta^{18}O$ contrast in benthic foraminifera to reconstruct deglacial evolution of atlantic meridional overturning circulation. *Paleoceanography and Paleoclimatology*, *34*(5), 800–812. https://doi.org/10.1029/2019PA003564

He, C., Liu, Z., Otto-Bliesner, B. L., Brady, E. C., Zhu, C., Tomas, R., et al. (2021a). Abrupt Heinrich Stadial 1 cooling missing in Greenland oxygen isotopes. *Science Advances*, *7*(25), eabh1007. https://doi.org/10.1126/sciadv.abh1007

He, C., Liu, Z., Otto-Bliesner, B. L., Brady, E. C., Zhu, C., Tomas, R., et al. (2021b). Hydroclimate footprint of pan-Asian monsoon water isotope during the last deglaciation. *Science Advances*, *7*(4), eabe2611. https://doi.org/10.1126/sciadv.abe2611

Hurrell, J. W., Holland, M. M., Gent, P. R., Ghan, S., Kay, J. E., Kushner, P. J., et al. (2013). The Community Earth System model: A framework for collaborative research. *Bulletin of the American Meteorological Society*, *94*(9), 1339–1360. https://doi.org/10.1175/BAMS-D-12-00121.1

Jacobs, S. S., Mele, P. A., Smethie, W. M., & Mortlock, R. A. (2005). *Summer oceanographic measurements near the Mertz Polynya (140-150E) on NB Palmer cruise 00-08* (p. 21). Lamont-Doherty Earth Observatory of Columbia University. Retrieved from http://www.nodc.noaa.gov/archive/arc0001/0001262/01-version/about/mdr.pdf

Jouzel, J., Masson-Delmotte, V., Cattani, O., Dreyfus, G., Falourd, S., Hoffmann, G., et al. (2007). Orbital and millennial Antarctic climate variability over the past 800,000 years. *Science*, *317*(5839), 793–796. https://doi.org/10.1126/science.1141038

Lamy, F., Arz, H. W., Kilian, R., Lange, C. B., Lembke-Jene, L., Wengler, M., et al. (2015). Glacial reduction and millennial-scale variations in Drake Passage throughflow. *Proceedings of the National Academy of Sciences*, *112*(44), 13496–13501. https://doi.org/10.1073/pnas.1509203112

Le Quere, C., Rodenbeck, C., Buitenhuis, E. T., Conway, T. J., Langenfelds, R., Gomez, A., et al. (2007). Saturation of the Southern Ocean CO_2 sink due to recent climate change. *Science*, *316*(5832), 1735–1738. https://doi.org/10.1126/science.1136188

LeGrande, A. N., & Schmidt, G. A. (2011). Water isotopologues as a quantitative paleosalinity proxy. *Paleoceanography*, *26*(3), PA3225. https://doi.org/10.1029/2010PA002043

Li, L., Lin, P., Yu, Y., Wang, B., Zhou, T., Liu, L., et al. (2013). The flexible global ocean-atmosphere-land system model, grid-point version 2: FGOALS-g2. *Advances in Atmospheric Sciences*, *30*(3), 543–560. https://doi.org/10.1007/s00376-012-2140-6

Li, L., Liu, Z., Zhu, C., He, C., & Otto-Bliesner, B. (2021). Shallowing glacial Antarctic intermediate water by changes in sea ice and hydrological cycle. *Geophysical Research Letters*, *48*(16). https://doi.org/10.1029/2021GL094317

Locarnini, R. A., Mishonov, A. V., Antonov, J. I., Boyer, T. P., Garcia, H. E., Baranova, O. K., et al. (2010). *World Ocean Atlas 2009, volume 1: Temperature (S. Levitus)*. NOAA Atlas NESDIS 68, U.S. Government Printing Office.

Lynch-Stieglitz, J. (2001). Using ocean margin density to constrain ocean circulation and surface wind strength in the past. *Geochemistry, Geophysics, Geosystems*, *2*(12). https://doi.org/10.1029/2001GC000208

Lynch-Stieglitz, J., Curry, W. B., Oppo, D. W., Ninneman, U. S., Charles, C. D., & Munson, J. (2006). Meridional overturning circulation in the South Atlantic at the last glacial maximum. *Geochemistry, Geophysics, Geosystems*, *7*(10). https://doi.org/10.1029/2005GC001226

Lynch-Stieglitz, J., Ito, T., & Michel, E. (2016). Antarctic density stratification and the strength of the circumpolar current during the Last Glacial Maximum. *Paleoceanography*, *31*(5), 539–552. https://doi.org/10.1002/2015PA002915

Marchitto, T. M., Curry, W. B., Lynch-Stieglitz, J., Bryan, S. P., Cobb, K. M., & Lund, D. C. (2014). Improved oxygen isotope temperature calibrations for cosmopolitan benthic foraminifera. *Geochimica et Cosmochimica Acta*, *130*, 1–11. https://doi.org/10.1016/j.gca.2013.12.034

Marshall, D. P., Ambaum, M. H. P., Maddison, J. R., Munday, D. R., & Novak, L. (2017). Eddy saturation and frictional control of the Antarctic Circumpolar Current. *Geophysical Research Letters*, *44*(1), 286–292. https://doi.org/10.1002/2016GL071702

Marshall, J., & Radko, T. (2003). Residual-mean solutions for the Antarctic circumpolar current and its associated overturning circulation. *Journal of Physical Oceanography*, *33*(11), 2341–2354. https://doi.org/10.1175/1520-0485(2003)033<2341:rsftac>2.0.co;2

McCave, I. N., Crowhurst, S. J., Kuhn, G., Hillenbrand, C.-D., & Meredith, M. P. (2014). Minimal change in Antarctic Circumpolar Current flow speed between the last glacial and holocene. *Nature Geoscience*, *7*(2), 113–116. https://doi.org/10.1038/ngeo2037

Miller, M. D., Simons, M., Adkins, J. F., & Minson, S. E. (2015). The information content of pore fluid δ18O and [Cl−]. *Journal of Physical Oceanography*, *45*(8), 2070–2094. https://doi.org/10.1175/JPO-D-14-0203.1

Olbers, D., Borowski, D., Völker, C., & Wölff, J.-O. (2004). The dynamical balance, transport and circulation of the Antarctic Circumpolar Current. *Antarctic Science*, *16*(4), 439–470. https://doi.org/10.1017/S0954102004002251

Orsi, A. H., Whitworth, T., & Nowlin, W. D. (1995). On the meridional extent and fronts of the Antarctic Circumpolar Current. *Deep Sea Research Part I: Oceanographic Research Papers*, *42*(5), 641–673. https://doi.org/10.1016/0967-0637(95)00021-W

Rintoul, S. R., Hughes, C., Olbers, D., Siedler, G., Church, J., & Gould, J. (2001). The Antarctic Circumpolar Current System. In *Ocean circulation and climate* (pp. 271–302). Academic Press. Retrieved from https://epic.awi.de/id/eprint/2649/1/Rin8888b.pdf https://doi.org/10.1016/s0074-6142(01)80124-8

Rintoul, S. R., & Sokolov, S. (2001). Baroclinic transport variability of the Antarctic Circumpolar Current south of Australia (WOCE repeat section SR3). *Journal of Geophysical Research*, *106*(C2), 2815–2832. https://doi.org/10.1029/2000JC900107

Sabine, C. L., Feely, R. A., Gruber, N., Key, R. M., Lee, K., Bullister, J. L., et al. (2004). The oceanic sink for anthropogenic CO2. *Science*, *305*(5682), 367–371. https://doi.org/10.1126/science.1097403

Schmidt, G. A., Bigg, G. R., & Rohling, E. J. (1999). *Global seawater oxygen-18 database—V1.22*. Retrieved from https://data.giss.nasa.gov/o18data/ https://doi.org/10.1023/a:1006043519663

Sigman, D. M., Hain, M. P., & Haug, G. H. (2010). The polar ocean and glacial cycles in atmospheric CO_2 concentration. *Nature*, *466*(7302), 47–55. https://doi.org/10.1038/nature09149

Smith, R., Jones, P., Briegleb, B., Bryan, F., Danabasoglu, G., Dennis, J., et al. (2010). *The Parallel Ocean Program (POP) reference manual: Ocean component of the community climate system model (CCSM)* (p. 141).

Snyder, C. W. (2016). Evolution of global temperature over the past two million years. *Nature*, *538*(7624), 226–228. https://doi.org/10.1038/nature19798

Sun, S., Eisenman, I., & Stewart, A. L. (2016). The influence of Southern Ocean surface buoyancy forcing on glacial-interglacial changes in the global deep ocean stratification. *Geophysical Research Letters*, *43*(15), 8124–8132. https://doi.org/10.1002/2016GL070058

Toyota, T., Smith, I. J., Gough, A. J., Langhorne, P. J., Leonard, G. H., Van Hale, R. J., et al. (2013). Oxygen isotope fractionation during the freezing of sea water. *Journal of Glaciology*, *59*(216), 697–710. https://doi.org/10.3189/2013JoG12J163

Voldoire, A., Sanchez-Gomez, E., Salas y Mélia, D., Decharme, B., Cassou, C., Sénési, S., et al. (2013). The CNRM-CM5.1 global climate model: Description and basic evaluation. *Climate Dynamics*, *40*(9), 2091–2121. https://doi.org/10.1007/s00382-011-1259-y

Watanabe, S., Hajima, T., Sudo, K., Nagashima, T., Takemura, T., Okajima, H., et al. (2011). MIROC-ESM 2010: Model description and basic results of CMIP5-20c3m experiments. *Geoscientific Model Development*, *4*(4), 845–872. https://doi.org/10.5194/gmd-4-845-2011

Wunsch, C. (1996). The ocean circulation inverse problem (Vol. 1–1, online resource (xiv, 442, [4] pages): illustrations, maps (some color)). Cambridge University Press. Retrieved from http://site.ebrary.com/id/10457355

Wunsch, C. (2016b). Last Glacial Maximum and deglacial abyssal seawater oxygen isotopic ratios. *Climate of the Past*, *12*(6), 1281–1296. https://doi.org/10.5194/cp-12-1281-2016

Wunsch, C. (2016a). Pore fluids and the LGM ocean salinity—Reconsidered. *Quaternary Science Reviews*, *135*, 154–170. https://doi.org/10.1016/j.quascirev.2016.01.015

Yukimoto, S., Adachi, Y., Hosaka, M., Sakami, T., Yoshimura, H., Hirabara, M., et al. (2012). A New Global Climate Model of the Meteorological Research Institute: MRI-CGCM3 —Model description and basic performance. *Journal of the Meteorological Society of Japan*, *90A*, 23–64. https://doi.org/10.2151/jmsj.2012-A02

Zhang, J., Liu, Z., Brady, E. C., Oppo, D. W., Clark, P. U., Jahn, A., et al. (2017). Asynchronous warming and δ18O evolution of deep Atlantic water masses during the last deglaciation. *Proceedings of the National Academy of Sciences*, *114*(42), 11075–11080. https://doi.org/10.1073/pnas.1704512114